

# Hydrophilic Character of Single-Layer MoS<sub>2</sub> Grown on Ag(111)

Francesco Tumino,<sup>\*,†</sup> Carlo Grazianetti,<sup>\*,‡</sup> Christian Martella,<sup>‡</sup> Marina Ruggeri,<sup>†</sup>  
Valeria Russo,<sup>†</sup> Andrea Li Bassi,<sup>†</sup> Alessandro Molle,<sup>‡</sup> and Carlo S. Casari<sup>†</sup>

<sup>†</sup>*Department of Energy, Politecnico di Milano, via G. Ponzio 34/3, Milano, I-20133, Italy*

<sup>‡</sup>*CNR-IMM Unit of Agrate Brianza, via C. Olivetti 2, Agrate Brianza, I-20864, Italy*

E-mail: francesco.tumino@polimi.it; cgrazianetti@mdm.imm.cnr.it

## Abstract

The study of MoS<sub>2</sub>/metal interfaces is crucial for engineering efficient semiconductor-metal contacts in 2D MoS<sub>2</sub>-based devices. Here we investigate a MoS<sub>2</sub>/Ag heterostructure fabricated by growing a single MoS<sub>2</sub> layer on Ag(111) by pulsed laser deposition under ultra-high vacuum (UHV) conditions. The surface structure is observed in-situ by scanning tunneling microscopy, revealing the hexagonal moiré pattern characteristic of the clean MoS<sub>2</sub>/Ag(111) interface. Ex-situ Raman spectroscopy reveals an anomalous behavior of vibrational modes, induced by the strong MoS<sub>2</sub>-Ag interaction. After few-hours exposure to ambient conditions the Raman response significantly changes and the formation of molybdenum oxysulfides is revealed by X-ray photoelectron spectroscopy. These effects are due to the interplay with water vapor and can be reversed by a moderate UHV annealing. A polymeric (PMMA) capping is demonstrated to hinder water-induced modifications, preserving the original interface quality for months.

# Introduction

In the last decade, molybdenum disulphide ( $\text{MoS}_2$ ) has been extensively studied as a promising 2D material for a wide range of potential applications, such as electronics, optoelectronics, catalysis and energy storage.<sup>1-3</sup> Among the many challenges in the route to develop novel  $\text{MoS}_2$ -based devices, the fabrication of efficient  $\text{MoS}_2$ -metal contacts is one of the most critical. Therefore, the study of  $\text{MoS}_2$ -metal heterostructures and their interface properties is necessary to provide a comprehensive understanding of the way  $\text{MoS}_2$  interacts with metals and how such interaction affects its electronic, phononic and transport properties. It is also crucial to assess the stability of  $\text{MoS}_2$ -metal systems by studying their chemical reactivity under ambient conditions, which can have profound effects on device performances.<sup>4-6</sup>

Recent works on  $\text{MoS}_2$ -metal heterostructures (mostly  $\text{MoS}_2$ -Au) have shown the influence of metallic contacts on electronic, optical and vibrational properties of  $\text{MoS}_2$ .<sup>7-13</sup> Such influence is related to metal-induced local strain and charge redistribution, and is dramatically dependent on the interface properties, especially in terms of purity and morphological homogeneity of the metal contact.<sup>7,14</sup> The ideal  $\text{MoS}_2$ -metal system, serving as model for fundamental studies, should have a contaminant-free, perfectly planar and atomically sharp interface. However, commonly employed fabrication techniques, like  $\text{MoS}_2$  exfoliation on metal substrates or physical vapor deposition (PVD) of metals on  $\text{MoS}_2$ , do not always comply with the above requirements: exfoliation being limited by unavoidable environmental contamination,<sup>14</sup> and PVD by the low metal wettability of  $\text{MoS}_2$ , which may lead to non-homogeneous contact.<sup>7</sup> An alternative and promising strategy relies on the synthesis of  $\text{MoS}_2$  on a perfectly clean and flat metallic surface under controlled growth conditions, e.g. using ultra-high vacuum (UHV) compatible techniques. However, synthesizing  $\text{MoS}_2$  on metal substrates with high control on its thickness down to the single-layer (SL) regime is still challenging, as the most widely used chemical vapor deposition (CVD) methods are largely limited to insulating or chemically inert substrates (e.g.  $\text{SiO}_2$ ).

In this work, we use UHV pulsed laser deposition (PLD) to grow SL  $\text{MoS}_2$  on Ag(111).

Our PLD method allows us to finely tune the MoS<sub>2</sub> coverage in the sub-monolayer range and thus to produce uniform SL MoS<sub>2</sub> films covering the Ag surface on the cm-scale. The morphological and structural properties are investigated down to the atomic scale by in-situ scanning tunneling microscopy (STM), revealing the characteristic moiré pattern due to the lattice mismatch between MoS<sub>2</sub> and Ag(111). Raman and photoluminescence (PL) spectroscopy (performed ex-situ) provide insight into the film-substrate interplay, revealing profound differences with respect to the well-known vibrational spectrum of SL MoS<sub>2</sub> supported by silica (or other dielectric substrates) and a complete quenching of the PL signal. The Raman spectrum is also used as fingerprint to monitor the effects of short-term exposure to ambient conditions, revealing a high sensitivity towards humidity. X-ray photoelectron spectroscopy (XPS) provides us with a more complete picture of the chemical behavior of the exposed heterostructure, corroborating the Raman analysis. We finally propose a polymer capping to preserve the original quality of MoS<sub>2</sub>/Ag(111) interface from degradation on the month time-scale, thus addressing a technologically relevant issue in the framework of 2D semiconductor-metal junctions.

## Methods

**Sample preparation and exposure** The synthesis and STM characterization of MoS<sub>2</sub>/Ag(111) was carried out in a UHV apparatus (at Politecnico di Milano, base pressure  $< 10^{-10}$  mbar) equipped with tools for surface preparation, and connected to a dedicated chamber for PLD (base pressure lower than  $5 \times 10^{-9}$  mbar). Ag(111)/mica (Mateck) was cleaned in the UHV chamber by cycles of Ar<sup>+</sup> sputtering (1 keV,  $3 \times 10^{-6}$ ) and annealing at 700 K. After having checked the Ag surface by STM, we internally transferred the substrate into the PLD chamber. MoS<sub>2</sub> was deposited at room temperature (RT), using KrF laser pulses (248 nm wavelength, 10 ns pulse duration) to ablate a stoichiometric MoS<sub>2</sub> target (Testbourne). The pulse energy was set at 200 mJ, yielding a laser fluence on the target of about 2 J/cm<sup>2</sup>.

The pulse repetition rate was set at 1 pulse/s, allowing us to easily control the total number of laser pulses. Target-substrate distance was set at 3 cm during depositions. The MoS<sub>2</sub> coverage was varied by properly tuning the number of laser pulses (between 3 and 15) on the target. After deposition, the sample was annealed at 730 K for 30 min in UHV and then observed by STM at RT. Once taken out from the UHV system, MoS<sub>2</sub>/Ag(111) samples were stored in ambient conditions inside simple transparent boxes to protect them from dust. Aged samples were restored to their original conditions by annealing them in UHV at 600 K for 2 hours. Sample exposure to O<sub>2</sub>, N<sub>2</sub> and H<sub>2</sub>O was performed in the load-lock chamber of the UHV system (base pressure  $5 \times 10^{-9}$  mbar). O<sub>2</sub> and N<sub>2</sub> were dosed at  $\sim 1$  bar using a needle valve. H<sub>2</sub>O was dosed using an electrically controlled leak valve. The volume of liquid water vaporized in the chamber roughly corresponds to the amount of water vapor in 75% humid air. The exposure time was set to 48 hours, enough to induce clearly observable modification in Raman spectra. After Raman measurements, the sample was put back in the UHV chamber, restored by annealing at 600 K for 2 hours and left cooled down to room temperature before exposing it to another gas.

**Scanning tunneling microscopy** In-situ STM measurements were performed at RT using an Omicron microscope. STM images were acquired in constant-current mode using homemade W tips, fabricated by electrochemical etching. Typical measurement parameters were in the range 0.5-2 V for bias voltage and 0.3-0.5 nA for set-point current.

**Raman spectroscopy** Raman measurements at Politecnico di Milano were performed in backscattering configuration using a Renishaw InVia spectrometer, coupled to an Ar laser. We used a 457 nm (2.71 eV) excitation, a 2400 lines/mm diffraction grating and a 50 $\times$  objective lens. The laser power on the sample was kept below 1 mW, taking care to avoid heating effects on the acquired spectra. We calibrated the spectrometer against the 521 cm<sup>-1</sup> peak of a Si crystal. The acquired spectra were baseline corrected and fitted using Voigt functions. We measured the photoluminescence (PL) signal with the same

instrument, using a 514 nm (2.41 eV) excitation and a 1800 lines/mm diffraction grating. Raman measurements at CNR were performed in backscattering configuration employing a Renishaw InVia spectrometer, equipped with the 514 nm (2.41 eV) line of solid-state diode laser and a 2400 lines/mm dispersive grating. The laser radiation was focused on the sample by means of a 50× Leica objective (0.75 numerical aperture), maintaining the incident laser power below 1 mW to avoid sample damage.

**X-ray photoelectron spectroscopy** XPS analysis was carried out in a second UHV apparatus (at CNR, base pressure  $10^{-10}$  mbar) by means of in situ non-monochromatized Mg X-ray source ( $h\nu = 1253.6$  eV) at  $37^\circ$  take-off angle (surface sensitive). The spectra were decomposed using a product between Gaussian and Lorentzian lineshapes upon Shirley background removal. The energy difference between the S  $2p$  (Mo  $3d$ ) spin-orbit doublet was kept equal to 1.172 eV (3.14 eV). The following core levels were recorded before and after UHV annealing and air exposure: S  $2p$ , Mo  $3d$  (plus S  $2s$ ), C  $1s$ , Ag  $3d$ , and O  $1s$ .

**Capping** A 9-6 wt.% poly (methyl methacrylate) (PMMA) solution was obtained dissolving PMMA (MicroChem, 950.000 MW) in anisole. The solution was stirred for 1h in a water bath at  $75^\circ\text{C}$ . A protective PMMA film was obtained by spin-coating a drop of solution on the sample surface at 6 krpm for 30 s.

## Results and Discussion

### Growth, morphology and structure

In the PLD process, the amount of deposited  $\text{MoS}_2$  can be controlled by tuning the number of laser pulses which ablate the  $\text{MoS}_2$  target. We started from a low number of pulses to study the first growth stages on Ag(111). With 3 laser pulses (figure 1a), and after annealing at 730 K in UHV, we observe the formation of 2D hexagonal shaped  $\text{MoS}_2$  nanoislands dispersed

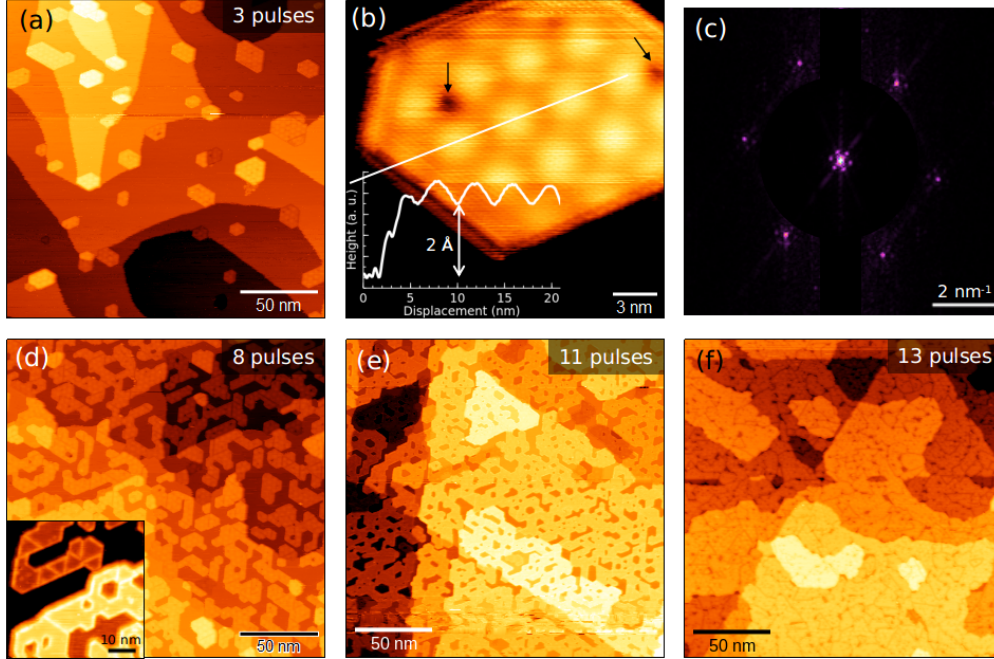


Figure 1: (a) Large-scale ( $200 \times 200 \text{ nm}^2$ ) STM image of SL MoS<sub>2</sub> nanocrystals on Ag(111), grown by PLD using 3 laser pulses. (b) High-resolution STM image of a SL MoS<sub>2</sub> nanocrystal. Black arrows indicate dark spots, presumably due to sulfur vacancies. Inset: line profile along the white line showing a 2 Å apparent height. (c) 2D Fourier Transform of the STM image in (b) showing both MoS<sub>2</sub> lattice and moiré spots. (d)-(f)  $200 \times 200 \text{ nm}^2$  STM images of SL MoS<sub>2</sub> on Ag(111) at different coverage. The three samples have been obtained by PLD with (d) 8, (e) 11 and (f) 13 laser pulses. (d)-Inset: STM image showing mirror boundaries between nanocrystals (bias voltage: -1.85 V, set-point current: 0.4 nA).

on the Ag surface. Most MoS<sub>2</sub> nanocrystals are attached to Ag step edges, suggesting that monoatomic steps provide preferential nucleation sites to MoS<sub>2</sub> growth. This mechanism is likely to limit the step mobility, leading to a more disordered step arrangement with respect to pristine Ag(111) (figure S1a). Figure 1b shows a high-resolution STM image of a MoS<sub>2</sub> nanocrystal. The measured apparent height is  $\sim 2 \text{ \AA}$  (see inset), which agrees with the STM thickness of a single MoS<sub>2</sub> layer grown on Au(111).<sup>13,15</sup> The surface shows a hexagonal moiré pattern with  $\sim 3.2 \text{ nm}$  periodicity, due to the lattice mismatch between MoS<sub>2</sub> and Ag(111) lattices. Fourier transforms of atomic resolution images (figure 1c) show that moiré and MoS<sub>2</sub> lattices are aligned, implying a negligible rotational mismatch between Ag(111) and MoS<sub>2</sub>. From the analysis of the moiré pattern,<sup>16</sup> we obtain a MoS<sub>2</sub> lattice parameter of  $3.17 \pm 0.02 \text{ \AA}$ , about 10% larger than the Ag(111) value, i.e.  $2.89 \text{ \AA}$ . The measured

lattice constant is close to the relaxed value of bulk MoS<sub>2</sub>, i.e. 3.16 Å.<sup>17</sup> However, the finite uncertainty in room-temperature STM measurements, albeit relatively small, does not allow us to exclude a possible residual strain in MoS<sub>2</sub> lattice (up to 1%), which may affect the vibrational properties, as discussed below. Dark spots (as those indicated by black arrows in figure 1b) are normally observed on MoS<sub>2</sub> surface. Comparably to MoS<sub>2</sub>/Au(111),<sup>18</sup> these features could be related to sulfur vacancies, the most common point defect in MoS<sub>2</sub>, which are normally promoted by UHV annealing.

Having synthesized and observed isolated SL MoS<sub>2</sub> nanocrystals on Ag(111), we aimed at increasing the MoS<sub>2</sub> coverage to obtain a continuous SL film. To this purpose, we gradually increased the number of laser pulses: in the bottom panel of figure 1 we report large-scale STM images acquired on three different samples obtained with 8 (d), 11 (e) and 13 (f) laser pulses. As coverage increases, the nanocrystals merge together into a connected SL structure, which gradually forms a uniform film on the Ag substrate (figure 1e-f). The MoS<sub>2</sub> lattice can grow on Ag(111) in two different orientations, rotated by 60° with each other. When differently oriented crystals merge together, they form mirror boundaries, which can be distinguished in STM images as straight lines between adjacent nanocrystals (figure 1d inset, at negative bias voltages the STM contrast of borders and mirror boundaries is normally enhanced). Therefore, the SL film is nanocrystalline, with mirror grain boundaries separating nano-sized domains. Second layer islands start growing only after the first layer is completed (figure S1b), suggesting a layer-by-layer growth mode driven by a strong film-substrate interaction (analogously to the PLD growth of SL MoS<sub>2</sub> on Au(111)<sup>13</sup>). Since we focused on the study of SL MoS<sub>2</sub>, we did not increase the coverage any further to avoid the presence of a significant fraction of second layer.

## Stability in ambient conditions

The SL MoS<sub>2</sub> film on Ag(111) was then investigated ex-situ by Raman spectroscopy, and constantly monitored to observe possible effects induced by air exposure over time. In the

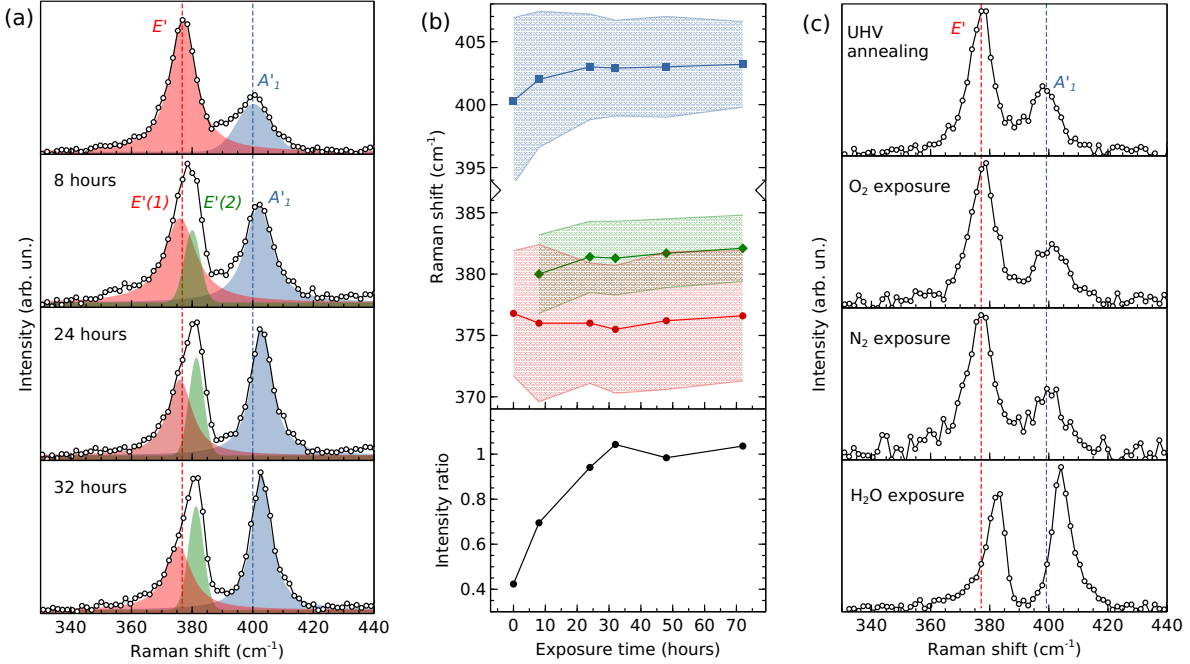


Figure 2: (a) Raman spectra of SL MoS<sub>2</sub>/Ag(111) acquired right after the sample was taken out from UHV (top), and after 8 (middle-top), 24 (middle-bottom) and 32 (bottom) hours of exposure to ambient conditions. Red, green and blue curves are Voigt functions fitting the Raman peaks. Vertical dashed lines indicate the peak positions of  $E'$  (red) and  $A'_1$  (blue). (b) Top: evolution of  $E'(1)$  (red),  $E'(2)$  (green) and  $A'_1$  (blue) peak positions and widths over exposure time. Color-shaded areas represent the FWHM of the Voigt components. Bottom: intensity ratio of the high-frequency over low-frequency peak ( $A'_1/E'$ ), reported as a function of air exposure time. (c) Raman spectra of SL MoS<sub>2</sub>/Ag(111) taken (top) after UHV annealing (600 K for 2 h) on a sample previously aged in air, and after 48 h exposure to O<sub>2</sub> (middle-top), N<sub>2</sub> (middle-bottom) and H<sub>2</sub>O (bottom). Vertical dashed lines indicate the peak positions of  $E'$  (red) and  $A'_1$  (blue).

top panel of figure 2a we report the Raman spectrum (457 nm excitation) obtained as soon as the sample was taken out from the UHV chamber. The plot shows the two main vibrational modes of SL MoS<sub>2</sub>, namely the in-plane mode  $E'$  at 376.8 cm<sup>-1</sup> and the out-of-plane  $A'_1$  at 400.3 cm<sup>-1</sup>. In the well-known spectrum of SL MoS<sub>2</sub> on SiO<sub>2</sub> (exfoliated or CVD-grown), the frequency difference between  $E'$  and  $A'_1$  is about 18-20 cm<sup>-1</sup> and the two modes are found at  $\sim 384$  cm<sup>-1</sup> and  $\sim 403$  cm<sup>-1</sup>, respectively.<sup>19</sup> The ratio of  $A'_1$  over  $E'$  intensity is  $\geq 1$  for a broad range of excitation wavelengths.<sup>20</sup> In comparison, SL MoS<sub>2</sub>/Ag(111) shows a downshift of both modes and a much lower  $A'_1/E'$  intensity ratio of  $\sim 0.4$ . Previous works have shown that strain<sup>21</sup> and doping<sup>22</sup> have considerable impact on MoS<sub>2</sub> Raman features.

In-plane biaxial strain mainly influences  $E'$ , which downshifts at a rate of  $\sim 5 \text{ cm}^{-1}$  per 1% of tensile strain, while  $\sim 2 \text{ cm}^{-1}/\%$  is the downshift rate for  $A'_1$ .<sup>7,21</sup> Using these values and the measured shift of  $E'$  and  $A'_1$ , we can infer a 1.4% in-plane biaxial tensile strain, which is approximately compatible with our STM measurements. However, the observed shifts can be further contributed by other effects, besides in-plane strain. For instance, the Ag(111) substrate may induce out-of-plane strain due to the interaction with contact S atoms, and n-type doping,<sup>23</sup> which is known to soften, broaden and damp the  $A'_1$  mode.<sup>22</sup> Both these mechanisms, concurrently with in-plane strain, can contribute to the anomalous Raman response observed on MoS<sub>2</sub>/Ag(111). Also, the strong photoluminescence signal associated to the direct gap of SL MoS<sub>2</sub> (e.g. detected on MoS<sub>2</sub> exfoliated on SiO<sub>2</sub><sup>24</sup>) is totally quenched on Ag(111) (figure S2), likely due to electron-hole separation favored by the metal contact.

After  $\sim 8$  hours in ambient conditions, we measured again the Raman spectrum (figure 2a, 8 hours panel). The low-frequency feature is now contributed by two peaks, referred to as  $E'(1)$  (red) and  $E'(2)$  (green), whose coexistence is discussed below. The high-frequency  $A'_1$  peak upshifts and its relative intensity increases. For increasing air exposure time (figure 2a, 24 and 32 hours panels),  $E'(2)$  and  $A'_1$  become more intense with respect to  $E'(1)$ , and upshift to  $\sim 382$  and  $\sim 403 \text{ cm}^{-1}$ , respectively (i.e. towards typical positions of SL MoS<sub>2</sub> on SiO<sub>2</sub>), while the frequency of  $E'(1)$  is essentially unvaried at  $376\text{-}377 \text{ cm}^{-1}$ . The observed behavior of MoS<sub>2</sub>/Ag(111) Raman modes is reported in figure 2b: the top panel shows  $E'(1)$ ,  $E'(2)$  and  $A'_1$  frequencies and linewidths as a function of air exposure time, while the bottom panel shows the measured ratio of  $A'_1$  intensity over the peak intensity (i.e. sum of  $E'(1)$  and  $E'(2)$ ) of the in-plane vibration. The most significant variations are observed within 48 hours of air exposure, after which an equilibrium situation is reached with the main peaks found at  $382.5$  and  $404 \text{ cm}^{-1}$ , and the  $A'_1/E'$  intensity ratio slightly above 1. At equilibrium, no significant changes are observed over one month (figure S3). The upshift of vibrational frequencies and the increase in intensity ratio suggest that the exposure to ambient conditions weakens the interaction between SL MoS<sub>2</sub> and Ag, responsible for the anomalous Raman

response observed on a pristine sample (figure 2a, top panel). In this picture, the coexistence of the two contributions,  $E'(1)$  and  $E'(2)$ , to the in-plane vibration can be attributed to the simultaneous sampling of two distinct types of regions within the laser spot (diameter of  $\sim 2 \mu\text{m}$  on the sample surface): a region where  $\text{MoS}_2$  strongly interacts with Ag and the other where such interaction is weaker. Thus, the gradual decrease of  $E'(1)$  against  $E'(2)$  over time suggests that the region of weak interaction becomes predominant over the other. Despite the evolution of vibrational properties, the PL signal is always totally quenched (figure S2), suggesting that a channel for charge separation or non-radiative decay is still active.

Aiming at restoring the original  $\text{MoS}_2$ -Ag interaction, we put the sample back in UHV and annealed it for 2 hours at 600 K. Once out the UHV system, its Raman spectrum (figure 2c, top) essentially overlaps with the pristine spectrum (figure 2a, top). This result proves that a mild annealing in UHV restores the condition prior to the short-term aging induced by air exposure. To deeper investigate the aging mechanism, we exposed the sample for 48 hours to controlled  $\text{O}_2$  (1 bar),  $\text{N}_2$  (1 bar) and  $\text{H}_2\text{O}$  (volume corresponding to 75% relative humidity, see Methods for further details) atmospheres, with the aim to possibly discriminate the different contributions of air components. The Raman spectra acquired ex-situ immediately after each exposure step are shown in figure 2c and labeled accordingly.  $\text{O}_2$  and  $\text{N}_2$  exposures do not induce any significant difference in the Raman spectrum of SL  $\text{MoS}_2/\text{Ag}(111)$ , whereas exposure to  $\text{H}_2\text{O}$  vapor results in the same variation of Raman modes discussed before. Our experiments thus point at humidity as the main cause for the short-term aging of SL  $\text{MoS}_2/\text{Ag}(111)$  in ambient conditions. Since the behavior of Raman modes can be associated with the weakening of  $\text{MoS}_2$ -Ag interaction, we argue that  $\text{H}_2\text{O}$  molecules gradually intercalate at the  $\text{MoS}_2/\text{Ag}$  interface, thus lifting  $\text{MoS}_2$  up from the metallic substrate. The intercalated regions increase over time, leading to the observed evolution of Raman features. Water intercalation caused by air exposure has been reported for SL  $\text{MoS}_2$  on hydrophilic dielectric substrates, e.g.  $\text{Al}_2\text{O}_3$ .<sup>25</sup> In our case, the intercalation could be favored by the hydrophilic character of  $\text{Ag}(111)$ .<sup>26</sup> Interestingly, we do not observe

any aging effects on SL MoS<sub>2</sub> grown on Au(111) using the same PLD method. Figure S4 shows the Raman spectra of MoS<sub>2</sub>/Au(111) as a function of air exposure time: the as-exposed spectrum (acquired as soon as the sample was taken out from UHV) is similar to the pristine MoS<sub>2</sub>/Ag(111) spectrum (figure 2a, top), but, in contrast to MoS<sub>2</sub>/Ag(111), no variations are observed for increasing exposure time. The different behavior of SL MoS<sub>2</sub>/Au(111) can be due to the low hydrophilicity of Au, which has lower water adsorption energy and wettability with respect to other metal surfaces.<sup>27-29</sup> This substrate effect corroborates the hypothesis that the aging of MoS<sub>2</sub>/Ag(111) is due to water intercalation, rather than e.g. water adsorption at the MoS<sub>2</sub> surface. The intercalation could be locally favored by the presence of defects, such as grain boundaries and sulfur vacancies (see figure 1b-d), which are known to enhance the local reactivity of TMDs in ambient conditions.<sup>30</sup>

XPS was carried out to study the chemical stability of MoS<sub>2</sub> on Ag(111). Figure 3a shows the S 2*p* (left) and Mo 3*d* (right) core levels after air exposure (less than 24 hours). The Mo 3*d* spectrum is nearly overlapped with the S 2*s* core level (orange line). The main doublet (red line) at binding energy (BE) 228.97 eV is related to the Mo<sup>4+</sup> ion of MoS<sub>2</sub> and is in good agreement with bulk reference (figure S5). The smaller doublet (red dashed curve) at 231.36 eV can be attributed to substoichiometric molybdenum oxysulphide (MoO<sub>*x*</sub>S<sub>*y*</sub>) because typically MoO<sub>3</sub> is found at higher BE (232.7 eV).<sup>31</sup> More interestingly even S 2*p* is composed of two distinct doublets. The former (red curve) at 161.87 eV is related to S<sup>2-</sup> state of MoS<sub>2</sub> (again in good agreement with bulk, figure S5), whereas the latter (red dashed) at lower BE (160.76 eV) deserves a deeper understanding and will be discussed in the following. After annealing the sample in UHV at 600 K for three hours (figure 3b), the low-BE S 2*p* doublet strongly decreases and shifts at higher BE, while the smaller MoO<sub>*x*</sub>S<sub>*y*</sub> doublet in the Mo 3*d* spectrum disappears. Therefore the emergence of both these features is related to air exposure and can be reversed by UHV annealing. In principle, the low-BE S 2*p* doublet could be associated to the possible formation of Ag<sub>2</sub>S<sup>32</sup> alloy, sulfur vacancies<sup>33</sup> or Mo-oxysulfides.<sup>34</sup> The hypothetical contribution of Ag<sub>2</sub>S can be ruled out by the following

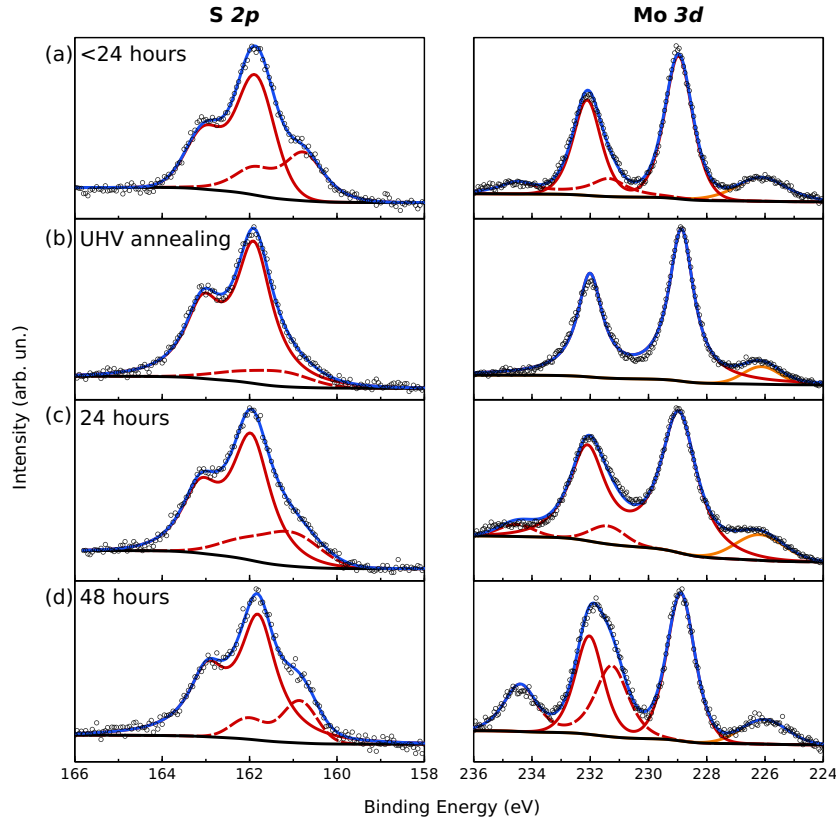


Figure 3: S  $2p$  (left) and Mo  $3d$  (right) core levels, where open circles are raw data, blue curve is the full fit after background removal (black curve), orange curve is S  $2s$  core level, red solid curves are  $\text{Mo}^{4+}$  and  $\text{S}^{2-}$  states for  $\text{MoS}_2$ , and red dashed curves are additional states discussed in main text, obtained: a) after less than 24 hours air exposure, b) after annealing in UHV for 3 hours at 600 K, c) after 24 hours air exposure, and d) after 48 hours air exposure (upon second annealing as in b).

evidences. First, the BE difference between the two S  $2p$  components is about 1 eV and such a difference is not observed in the Ag  $3d$  core level, whose BE and lineshape are unaffected by UHV annealing or air exposure (data not shown). Second, the observed exposure/annealing behavior would lead to the counterintuitive conclusion that  $\text{Ag}_2\text{S}$  alloying results from air exposure and is reversed by UHV annealing. The latter argument allows us to rule out also the possible contribution of S vacancies, whose formation/removal could be hardly correlated to the exposure/annealing cycle. Therefore, we attribute the low-BE S  $2p$  component to the formation of Mo-oxysulfide compounds,<sup>34</sup> also responsible for the high-BE doublet of Mo  $3d$ , as pointed out before.

The annealed sample is then exposed to air for 24 hours (figure 3c), thus recovering the Mo 3*d* and S 2*p* spectra of figure 3a. The same sample is then annealed again at the same temperature (600 K) and subsequently exposed for 48 hours (figure 3d). The low-BE S 2*p* doublet is fully restored (as in figure 3a) and the high-BE of the Mo 3*d* line noticeably increases. Comparing the O 1*s* spectra after 24 and 48 hours (figure S6), we observe an increase of a high-BE component typically related to hydroxyl groups (OH), compatible with reported MoO<sub>*y*</sub>S<sub>*z*</sub> compound with oxygen-rich composition.<sup>34</sup> The gradual formation of a MoO<sub>*x*</sub>S<sub>*y*</sub> phase, mediated by reactive hydroxyl groups, further confirms the time-dependent interaction between water vapor and MoS<sub>2</sub>/Ag. The possibility to restore the original condition by UHV annealing suggests that hydroxyl groups are weakly bounded and can be removed to recover the pristine MoS<sub>2</sub>-Ag interface.

To prevent sample aging, we adopted the following strategy aiming at hindering water intercalation at the MoS<sub>2</sub>-Ag interface. After annealing the sample in UHV for 2 hours to restore the MoS<sub>2</sub>-Ag interaction (confirmed by means of Raman investigation), we spin-coated PMMA on the sample surface obtaining a capping film. At variance with the analysis reported in figure 2a, the Raman spectra of the PMMA-capped MoS<sub>2</sub> turn out to be unaffected by the environmental humidity even after one month of ambient condition exposure (figure S7). More in detail, in terms of time evolution, the characteristic *E'* and *A*<sub>1</sub>' Raman modes show neither the frequency upshift nor the relative intensity switch exhibited by the uncapped sample. As a matter of fact, the *A*<sub>1</sub>'/*E'* intensity ratio is constantly below 1 throughout the considered temporal window. We concluded that the PMMA capping layer is effective in creating a barrier against water intercalation, thus preserving the strong MoS<sub>2</sub>-Ag interaction, observed in the pristine sample, on a time scale of months.

## Conclusions

In conclusion, we synthesized SL MoS<sub>2</sub> on Ag(111) by PLD, observed its structure by in-situ STM and studied its stability by Raman spectroscopy and XPS. The moiré pattern observed on pristine MoS<sub>2</sub>/Ag(111) is indicative of the high-purity interface obtained with the employed UHV-PLD scheme, a condition proved to be relevant for the fabrication of low-resistance contacts.<sup>35</sup> The strong interaction with the metallic substrate has profound effects in MoS<sub>2</sub> Raman modes, whose frequencies and intensities are affected by strain and doping induced by the Ag substrate. Air exposure affects the chemical stability of SL MoS<sub>2</sub>/Ag(111) over a time-scale of a few hours. The main aging mechanism is identified in water intercalation at the MoS<sub>2</sub>/Ag interface, causing the formation of Mo-oxysulfides, which can be reversed by UHV annealing. A PMMA capping layer, applied immediately after air exposure, efficiently protects the sample from water, preventing the related aging. Our findings clearly show the influence of the Ag substrate on the properties of SL MoS<sub>2</sub>, along with the importance of interface effects in the heterostructure stability. This work deepens our understanding of TMD/metal systems providing relevant insight into their interface physics, which plays a pivotal role in the performances of TMD devices.

## Acknowledgement

F.T., V.R., A.L.B., C.S.C. acknowledge funding from the European Research Council (ERC) under the European Union's Horizon 2020 research and innovation programme ERC-Consolidator Grant (ERC CoG 2016 EspLORE grant agreement no. 724610, website: [www.esplora.polimi.it](http://www.esplora.polimi.it)). C.G., C.M. and A.M. acknowledge funding from the ERC under the European Union's Horizon 2020 research and innovation programme ERC-Consolidator Grant (ERC CoG Xfab grant agreement no. 772261, website: [xfab.mdm.imm.cnr.it](http://xfab.mdm.imm.cnr.it)).

## Supporting Information Available

Additional STM, Raman, photoluminescence and XPS data.

## References

- (1) Jariwala, D.; Sangwan, V. K.; Lauhon, L. J.; Marks, T. J.; Hersam, M. C. Emerging device applications for semiconducting two-dimensional transition metal dichalcogenides. *ACS Nano* **2014**, *8*, 1102–1120.
- (2) Bang, G. S.; Nam, K. W.; Kim, J. Y.; Shin, J.; Choi, J. W.; Choi, S.-Y. Effective liquid-phase exfoliation and sodium ion battery application of MoS<sub>2</sub> nanosheets. *ACS Appl. Mater. Interfaces* **2014**, *6*, 7084–7089.
- (3) Yan, Y.; Xia, B.; Ge, X.; Liu, Z.; Wang, J.-Y.; Wang, X. Ultrathin MoS<sub>2</sub> nanoplates with rich active sites as highly efficient catalyst for hydrogen evolution. *ACS Appl. Mater. Interfaces* **2013**, *5*, 12794–12798.
- (4) Qiu, H.; Pan, L.; Yao, Z.; Li, J.; Shi, Y.; Wang, X. Electrical characterization of back-gated bi-layer MoS<sub>2</sub> field-effect transistors and the effect of ambient on their performances. *Appl. Phys. Lett.* **2012**, *100*, 123104.
- (5) Tongay, S.; Zhou, J.; Ataca, C.; Liu, J.; Kang, J. S.; Matthews, T. S.; You, L.; Li, J.; Grossman, J. C.; Wu, J. Broad-range modulation of light emission in two-dimensional semiconductors by molecular physisorption gating. *Nano Lett.* **2013**, *13*, 2831–2836.
- (6) Late, D. J.; Liu, B.; Matte, H. R.; Dravid, V. P.; Rao, C. Hysteresis in single-layer MoS<sub>2</sub> field effect transistors. *ACS Nano* **2012**, *6*, 5635–5641.
- (7) Gong, C.; Huang, C.; Miller, J.; Cheng, L.; Hao, Y.; Cobden, D.; Kim, J.; Ruoff, R. S.; Wallace, R. M.; Cho, K., et al. Metal contacts on physical vapor deposited monolayer MoS<sub>2</sub>. *ACS Nano* **2013**, *7*, 11350–11357.

- (8) Sun, Y.; Liu, K.; Hong, X.; Chen, M.; Kim, J.; Shi, S.; Wu, J.; Zettl, A.; Wang, F. Probing local strain at MX<sub>2</sub>–metal boundaries with surface plasmon-enhanced Raman scattering. *Nano Lett.* **2014**, *14*, 5329–5334.
- (9) Yuan, H.; Cheng, G.; You, L.; Li, H.; Zhu, H.; Li, W.; Kopanski, J. J.; Obeng, Y. S.; Hight Walker, A. R.; Gundlach, D. J., et al. Influence of metal–MoS<sub>2</sub> interface on MoS<sub>2</sub> transistor performance: Comparison of Ag and Ti contacts. *ACS Appl. Mater. Interfaces* **2015**, *7*, 1180–1187.
- (10) Rahaman, M.; Rodriguez, R. D.; Plechinger, G.; Moras, S.; Schüller, C.; Korn, T.; Zahn, D. R. Highly localized strain in a MoS<sub>2</sub>/Au heterostructure revealed by tip-enhanced Raman spectroscopy. *Nano Lett.* **2017**, *17*, 6027–6033.
- (11) Velicky, M.; Rodriguez, A.; Bousa, M.; Krayev, A. V.; Vondracek, M.; Honolka, J.; Ahmadi, M.; Donnelly, G. E.; Huang, F.; Abruña, H. D., et al. Strain and charge doping fingerprints of the strong interaction between monolayer MoS<sub>2</sub> and gold. *J. Phys. Chem. Lett.* **2020**, *11*, 6112–6118.
- (12) Petó, J.; Dobrik, G.; Kukucska, G.; Vancsó, P.; Koós, A. A.; Koltai, J.; Nemes-Incze, P.; Hwang, C.; Tapasztó, L. Moderate strain induced indirect bandgap and conduction electrons in MoS<sub>2</sub> single layers. *npj 2D Mater. Appl.* **2019**, *3*, 1–6.
- (13) Tumino, F.; Casari, C.; Passoni, M.; Bottani, C.; Bassi, A. L. Pulsed Laser Deposition of Two-Dimensional ZnO Nanocrystals on Au(111): Growth, Surface Structure and Electronic Properties. *Nanotechnology* **2016**, *27*, 475703.
- (14) Velicky, M.; Donnelly, G. E.; Hendren, W. R.; McFarland, S.; Scullion, D.; DeBenedetti, W. J.; Correa, G. C.; Han, Y.; Wain, A. J.; Hines, M. A., et al. Mechanism of gold-assisted exfoliation of centimeter-sized transition-metal dichalcogenide monolayers. *ACS Nano* **2018**, *12*, 10463–10472.

- (15) Sørensen, S. G.; Füchtbauer, H. G.; Tuxen, A. K.; Walton, A. S.; Lauritsen, J. V. Structure and electronic properties of in situ synthesized single-layer MoS<sub>2</sub> on a gold surface. *ACS Nano* **2014**, *8*, 6788–6796.
- (16) N'Diaye, A. T.; Coraux, J.; Plasa, T. N.; Busse, C.; Michely, T., et al. Structure of epitaxial graphene on Ir(111). *New J. Phys.* **2008**, *10*, 043033.
- (17) Wilson, J. A.; Yoffe, A. The transition metal dichalcogenides discussion and interpretation of the observed optical, electrical and structural properties. *Adv. Phys.* **1969**, *18*, 193–335.
- (18) Tumino, F.; Casari, C. S.; Li Bassi, A.; Tosoni, S. Nature of point defects in single-layer MoS<sub>2</sub> supported on Au(111). *J. Phys. Chem. C* **2020**, *124*, 12424–12431.
- (19) Zhang, X.; Qiao, X.-F.; Shi, W.; Wu, J.-B.; Jiang, D.-S.; Tan, P.-H. Phonon and Raman scattering of two-dimensional transition metal dichalcogenides from monolayer, multilayer to bulk material. *Chem. Soc. Rev.* **2015**, *44*, 2757–2785.
- (20) Carvalho, B. R.; Malard, L. M.; Alves, J. M.; Fantini, C.; Pimenta, M. A. Erratum: Symmetry-dependent exciton-phonon coupling in 2D and bulk MoS<sub>2</sub> observed by resonance Raman scattering [Phys. Rev. Lett. 114, 136403 (2015)]. *Phys. Rev. Lett.* **2016**, *116*, 089904.
- (21) Lloyd, D.; Liu, X.; Christopher, J. W.; Cantley, L.; Wadehra, A.; Kim, B. L.; Goldberg, B. B.; Swan, A. K.; Bunch, J. S. Band gap engineering with ultralarge biaxial strains in suspended monolayer MoS<sub>2</sub>. *Nano Lett.* **2016**, *16*, 5836–5841.
- (22) Chakraborty, B.; Bera, A.; Muthu, D.; Bhowmick, S.; Waghmare, U. V.; Sood, A. Symmetry-dependent phonon renormalization in monolayer MoS<sub>2</sub> transistor. *Phys. Rev. B* **2012**, *85*, 161403.

- (23) Gong, C.; Colombo, L.; Wallace, R. M.; Cho, K. The unusual mechanism of partial Fermi level pinning at metal–MoS<sub>2</sub> interfaces. *Nano Lett.* **2014**, *14*, 1714–1720.
- (24) Mak, K. F.; Lee, C.; Hone, J.; Shan, J.; Heinz, T. F. Atomically thin MoS<sub>2</sub>: a new direct-gap semiconductor. *Phys. Rev. Lett.* **2010**, *105*, 136805.
- (25) Zheng, C.; Xu, Z.-Q.; Zhang, Q.; Edmonds, M. T.; Watanabe, K.; Taniguchi, T.; Bao, Q.; Fuhrer, M. S. Profound effect of substrate hydroxylation and hydration on electronic and optical properties of monolayer MoS<sub>2</sub>. *Nano Lett.* **2015**, *15*, 3096–3102.
- (26) Osman, M. A.; Keller, B. A. Wettability of native silver surfaces. *Appl. Surf. Sci.* **1996**, *99*, 261–263.
- (27) Meng, S.; Kaxiras, E.; Zhang, Z. Water wettability of close-packed metal surfaces. *J. Chem. Phys.* **2007**, *127*, 244710.
- (28) Möller, C.; Barreto, J.; Stavale, F.; Tissot, H.; Shaikhutdinov, S.; Freund, H.-J.; Nil-  
ius, N. Water adsorption to crystalline Cu<sub>2</sub>O thin films: Structural and vibrational properties. *J. Phys. Chem. C* **2018**, *122*, 2195–2199.
- (29) Michaelides, A.; Ranea, V.; De Andres, P.; King, D. General model for water monomer adsorption on close-packed transition and noble metal surfaces. *Phys. Rev. Lett.* **2003**, *90*, 216102.
- (30) Kotsakidis, J. C.; Zhang, Q.; Vazquez de Parga, A. L.; Currie, M.; Helmerson, K.; Gaskill, D. K.; Fuhrer, M. S. Oxidation of monolayer WS<sub>2</sub> in ambient is a photoinduced process. *Nano Lett.* **2019**, *19*, 5205–5215.
- (31) Weber, T.; Muijsers, J.; Van Wolput, J.; Verhagen, C.; Niemantsverdriet, J. Basic reaction steps in the sulfidation of crystalline MoO<sub>3</sub> to MoS<sub>2</sub>, as studied by X-ray photoelectron and infrared emission spectroscopy. *J. Phys. Chem.* **1996**, *100*, 14144–14150.

- (32) Kaushik, V. K. XPS core level spectra and Auger parameters for some silver compounds. *J. Electron Spectrosc. Relat. Phenom.* **1991**, *56*, 273–277.
- (33) Donarelli, M.; Bisti, F.; Perrozzi, F.; Ottaviano, L. Tunable sulfur desorption in exfoliated MoS<sub>2</sub> by means of thermal annealing in ultra-high vacuum. *Chem. Phys. Lett.* **2013**, *588*, 198–202.
- (34) Benoist, L.; Gonbeau, D.; Pfister-Guillouzo, G.; Schmidt, E.; Meunier, G.; Levasseur, A. X-ray photoelectron spectroscopy characterization of amorphous molybdenum oxysulfide thin films. *Thin Solid Films* **1995**, *258*, 110–114.
- (35) Smithe, K. K.; Suryavanshi, S. V.; Munoz Rojo, M.; Tedjarati, A. D.; Pop, E. Low variability in synthetic monolayer MoS<sub>2</sub> devices. *ACS Nano* **2017**, *11*, 8456–8463.

# Graphical TOC Entry

